IOP PUBLISHING PHYSICS IN MEDICINE AND BIOLOGY

Phys. Med. Biol. **53** (2008) 1325–1351 doi:10.1088/0031-9155/53/5/011

Investigation of the signal behavior at diagnostic energies of prototype, direct detection, active matrix, flat-panel imagers incorporating polycrystalline HgI_2

Hong Du, Larry E Antonuk, Youcef El-Mohri, Qihua Zhao, Zhong Su[1], Jin Yamamoto[2] and Yi Wang

Department of Radiation Oncology, University of Michigan Medical Center, Ann Arbor, Michigan 48109, USA

E-mail: antonuk@umich.edu

Received 30 September 2007, in final form 20 January 2008
Published 14 February 2008
Online at stacks.iop.org/PMB/53/1325

Abstract

Active matrix, flat-panel x-ray imagers based on a-Si:H thin-film transistors offer many advantages and are widely utilized in medical imaging applications. Unfortunately, the detective quantum efficiency (DQE) of conventional flat-panel imagers incorporating scintillators or a-Se photoconductors is significantly limited by their relatively modest signal-to-noise ratio, particularly in applications involving low x-ray exposures or high spatial resolution. For this reason, polycrystalline HgI_2 is of considerable interest by virtue of its low effective work function, high atomic number and the possibility of large-area deposition. In this study, a detailed investigation of the properties of prototype, flat-panel arrays coated with two forms of this high-gain photoconductor are reported. Encouragingly, high x-ray sensitivity, low dark current and spatial resolution close to the theoretical limits were observed from a number of prototypes. In addition, input-quantum-limited DQE performance was measured from one of the prototypes at relatively low exposures. However, high levels of charge trapping, lag and polarization, as well as pixel-to-pixel variations in x-ray sensitivity are of concern. While the results of the current study are promising, further development will be required to realize prototypes exhibiting the characteristics necessary to allow practical implementation of this approach.

1. Introduction

Active matrix flat panel imager (AMFPI) technology has undergone extensive research and development since its conception in the late 1980s (Street *et al* 1990, Antonuk *et al* 1991).

[1] Currently at the Department of Radiation Oncology, Virginia Commonwealth University,VA, USA.
[2] Currently at Microsoft Corporation, One Microsoft Way, Redmond, WA, USA.

AMFPIs employ a two-dimensional matrix of a-Si:H thin-film transistors (TFTs), connected to gate and data address lines. These circuits are fabricated on large glass substrates to form pixelated arrays and may be divided into two categories: direct detection and indirect detection. Direct detection imagers use a photoconductor (a-Se) to convert x-rays directly into pixel charge signal while indirect detection imagers use scintillators (e.g. CsI:Tl) to convert x-rays into optical photons which, in turn, are converted into pixel signal by a photosensor integrated into each pixel.

AMFPIs offer many advantages over conventional analog x-ray imaging technologies, including real-time operation and high quality, large area digital images. These devices have been successfully introduced to many medical x-ray imaging applications including radiotherapy, angiography, radiography, fluoroscopy and mammography (Antonuk *et al* 1998, Granfors *et al* 2003, Samei and Flynn 2003, Zhao *et al* 2003, Vedantham *et al* 2000). However, for applications involving low exposure or high spatial resolution, the performance of AMFPIs, quantified in terms of the detective quantum efficiency (DQE), degrades due to the relatively high level of additive noise compared to the pixel x-ray signal (Antonuk *et al* 2000, Zhao and Zhao 2003, El-Mohri *et al* 2007, Maolinbay *et al* 2000).

To overcome this limitation, significant improvement in the signal-to-noise ratio (SNR) of AMFPIs is required and a variety of strategies have been proposed to accomplish this goal by enhancing the amount of signal generated in, and extracted from each pixel per interacting x-ray—given that significant reductions in additive noise appear unlikely. One approach for enhancing signal gain involves replacement of the discrete photodiodes used in conventional indirect detection AMFPIs with a continuous photodiode structure to improve the fraction of the optically sensitive area in each pixel (El-Mohri *et al* 2007). Another approach for providing a greater degree of gain enhancement, which could be applied to both direct and indirect detection imagers, involves integration of in-pixel amplifier circuits, based on a-Si:H or polycrystalline silicon thin-film transistors (Matsuura *et al* 1999, Antonuk *et al* 2000, Karim *et al* 2003), and functional, prototype, indirect detection arrays of the latter design have been reported (Antonuk *et al* 2005). In addition, the feasibility of significant gain enhancement through incorporation of an a-Se avalanche photoconductor is under investigation (Zhao *et al* 2005, Hunt *et al* 2007).

Another strategy for improving SNR, and thereby DQE performance, of direct detection AMFPIs involves the use of photoconductive materials, such as PbI_2, HgI_2 and PbO, which provide a significantly higher signal per unit of absorbed x-ray energy than that of the a-Se photoconductors currently used in commercial direct detection devices (Street *et al* 2002, Zentai *et al* 2007, Zuck *et al* 2003, Hartsough *et al* 2004, Simon *et al* 2005). As is the case for a-Se, there is no reported fundamental limitation on the maximum area for any of these photoconductive materials. HgI_2, in particular, exhibits a number of interesting properties, making it an attractive candidate. With a high atomic number and mass density, relatively high detection efficiencies at diagnostic energies can be achieved with film thicknesses of only 300 to 500 μm (Su *et al* 2005). Moreover, recent investigations of polycrystalline HgI_2 have demonstrated that this material offers an attractively low effective work function, W_{EFF}. (In the present context, W_{EFF} is defined as the average amount of absorbed x-ray energy required to generate one unit of detected pixel charge.) Values for W_{EFF} of $\sim$5 eV have been reported for polycrystalline HgI_2 (Su *et al* 2005, Street *et al* 2002) at far lower electric field strengths (less than 1 V μm^{-1}) than the $\sim$10 V μm^{-1} required to obtain a W_{EFF} of $\sim$50 eV for a-Se. Thus, a far thinner layer of HgI_2 can be used to detect a given fraction of incident x-rays, and at a much lower electric field compared to an a-Se detector (Zentai *et al* 2002, Antonuk *et al* 2004).

In this paper, we investigate direct detection AMFPIs incorporating polycrystalline HgI_2. The reported results were obtained from a relatively large number of prototype arrays coated with two types of HgI_2. This study was undertaken with the goal of exploring properties and behaviors that affect imager performance through the systematic evaluation of pixel dark current, dark signal drift, x-ray signal sensitivity, W_{EFF}, non-uniformity, charge trapping, lag and modulation transfer function (MTF). Higher level performance metrics, noise power spectra (NPS) and DQE, obtained from one of the better performing prototypes, are also presented, and comparisons of these DQE results with calculations from a cascaded systems analysis are made. Finally, prospects for future development of this approach, including challenges to be met, are discussed.

2. Devices and methodology

2.1. HgI_2 fabrication

For this study, fabrication of polycrystalline HgI_2 film was performed by real-time radiography (RTR, Israel) using two low temperature deposition methods—physical vapor deposition (PVD) and particle-in-binder deposition (PIB). (Schieber *et al* 1999, 2001) PVD deposition was performed in a vacuum reactor where high purity HgI_2 powder was evaporated and deposited on arrays. The temperatures used during deposition were chosen based on a number of criteria, most importantly to encourage the c-axis of the crystal to grow perpendicularly to the array surface and to keep the temperature well below a value ($\sim$230 °C) at which damage to the arrays would occur. PIB deposition involves grains of purified HgI_2 crystals ($\sim$6.36 g cm^{-3}) mixed with a polymer binder material ($\sim$1.05 g cm^{-3}), with a composition ratio of 9 to 1 by weight for the two materials. It is desirable that the polymer has approximately the same electrical resistance as that of HgI_2, so as to facilitate the flow of x-ray-induced charge across the boundaries between HgI_2 grains and the polymer. The mixture of HgI_2 and binder is first made into a slurry by adding a solvent, and then deposited onto the surface of an array. The solvent was subsequently evaporated using a low temperature sintering process. The packing density, defined as the percent of the mass density of HgI_2 in the film relative to the single crystal density of the material, was $\sim$90% and 50% for PVD and PIB, respectively.

2.2. Array designs

A pair of similar direct detection array designs, referred to as ND10 and MD88 (dpiX, USA), with a 127 μm pixel pitch were used in this study. These designs are based on a conventional pixel structure, with each pixel consisting of a single a-Si:H TFT coupled to a charge storage capacitor. Specifications for the designs are listed in table 1. Beyond the difference in pixel format (768 $\times$ 768 versus 1024 $\times$ 1024), the major difference between the two designs is the surface topology. Due to suspicions that non-planar features on the top surface of an uncoated array may tend to disrupt the orderly growth of PVD HgI_2, thereby increasing dark current, the newer MD88 arrays were made more uniform. Specifically, a depression in the array surface due to a 'via' (the small opening in the passivation layer allowing a metallic electrical connection to be established between the collection electrode and the top plate of the pixel storage capacitor, as illustrated in figure 1(c)), was reduced from $\sim$40 $\times$ 40 μm^2 with a depth of $\sim$2.6 μm for ND10 to $\sim$6 $\times$ 6 μm^2 with a depth of $\sim$2.0 μm for MD88.

Microphotographs of a single pixel from an ND10 and an MD88 array are shown in figures 1(a) and 1(b), respectively. The geometric fill factor, defined as the fraction of pixel area occupied by the collection electrode, is $\sim$79% and 83%, for ND10 and MD88,

Table 1. Specifications, operational conditions and properties of the two AMFPI array designs used in these studies. See the text for further details.

Array design	ND10	MD88
Pixel pitch (μm)	127	127
Pixel format	768 × 768	1024 × 1024
Array dimension (cm^2)	9.8 × 9.8	13.0 × 13.0
TFT dimensions, W/L (μm /μm)	20/9.5	24/8
Pixel storage capacitance (pF)	1.13	1.05
Data line capacitance (pF)	∼30	∼34
Geometric fill factor	79%	83%
Area of via depression (μm^2)	40 × 40	6 × 6
Depth of via depression (μm)	2.6	2.0
TFT gate-on/off voltage (V)	10/−8	10/−8
Storage capacitor ground voltage (V)	−8	−6
TFT off current (fA)	∼3	∼21
TFT on resistance (MΩ)	2.6	3.9
TFT threshold voltage (V)	1.2 to 2.1	1.2 to 2.1
a-Si carrier mobility (cm^2 V^{-1} s^{-1})	0.54 to 0.74	0.45 to 0.65

respectively. The geometry of the collection electrode is designed to have a minimal overlap with the gate lines and data lines in order to reduce capacitive coupling. Note that, although the collection electrode (indicated by the dashed lines) does not cover the entire pixel area, the effective charge collection fill factor has been demonstrated to be close to the maximally attainable value of 100% for similar direct detection array designs (Street *et al* 2002, Zhao *et al* 2003) and thus is assumed to be the case for the present array designs.

Compared to other photoconductive materials such as a-Se and PbI_2, HgI_2 is very chemically active and reacts with metals (e.g. Al) commonly used in AMFPI arrays. Such reactions can, over the course of hours to months, create significant numbers of defective address lines and pixels. While those metals in the array that could react with HgI_2 were, in principle, protected by an overlying passivation layer, the aluminum surface of the peripheral contact pads had to be carefully shielded during photoconductor deposition.

2.3. Construction of photoconductive detectors

To create the prototype arrays evaluated in this study, construction of x-ray detector structures on uncoated arrays was performed at RTR and involved the following steps: (a) deposition of a thin polymer barrier layer on the surface of the array; (b) deposition of a layer of polycrystalline PVD or PIB HgI_2; (c) deposition of a thin metal layer (∼1000 Å of palladium) to form a top electrode to allow an electric field to be applied across the HgI_2 layer using a high voltage power supply; and (d) encapsulation of the array with an ∼7 μm thick polymer layer to protect the surface and to prevent evaporation of HgI_2. The barrier layer is designed with a number of objectives. It should inhibit chemical reactions between HgI_2 and aluminum in the underlying array and provide adhesion of the photoconductor to the array surface. It must also allow the transport of charge induced by x-rays from the photoconductor to the underlying pixel collection electrodes. However, it is important that the barrier layer does not allow charge sharing between the collection electrodes of neighboring pixels. The thickness of the barrier layer was chosen to be ∼1.5 and 3.0 μm for PVD and PIB depositions, respectively. A thicker barrier layer was chosen for the PIB depositions in an attempt to protect the underlying array from the solvent in the PIB slurry, which tends to penetrate into the barrier material and could potentially affect array performance. The two major types of barrier layer used, labeled

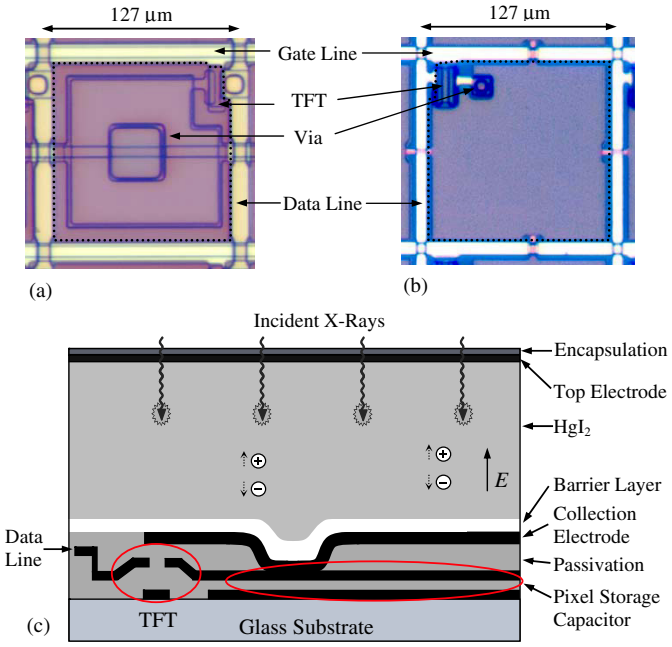

Figure 1. Microphotographs of the top surface of (a) an ND10 pixel and (b) an MD88 pixel. These images were acquired prior to the deposition of the materials comprising a HgI_2 detector (i.e., the barrier layer, the photoconductor, the top electrode and an encapsulation layer). The dashed lines superimposed on the photos indicate the periphery of the signal collection electrode. (c) Schematic cross-sectional view of an ND10 pixel with a HgI_2 detector—where the drawing has not been made to scale in order to better illustrate various features of the pixel designs. The cross-sectional view for an MD88 pixel would generally look the same except that the collection electrode also serves as the top electrode of the pixel storage capacitor and this electrode is connected by a via to the drain contact of the TFT. Note that, in this drawing, the depression illustrated in the otherwise planar collection electrode corresponds to an $\sim 40 \times 40\ \mu m^2$ large, $\sim 2.6\ \mu m$ deep depression located on the surface of the bare ND10 pixel—a feature that is located at the position of the via indicated in (a).

A and D, were based on different polymers and correspond to those reported in an earlier study of the signal properties of simple, non-pixelated film detectors (Su *et al* 2005). The variations in barrier type D (designated by number codes following the letter, see table 2) correspond to deliberate changes in conductivity. (The manufacturer declined to disclose further information about the barrier layers for proprietary reasons.)

For all prototypes, the HgI_2 deposition thickness was quite uniform, with variations of no more than 10% across the array surface, as indicated by the manufacturer. Figure 1(c) shows a schematic view of the pixel structure of a direct detection array incorporating HgI_2. As illustrated in this figure, incident x-rays interact with HgI_2, generating electron–hole pairs. The electrons and holes are swept by the electric field generated by means of a negative bias voltage applied to the top electrode, thereby creating pixel signal in the storage capacitor.

2.4. Prototype arrays investigated in this study

To explore the properties and behaviors that affect HgI_2 imager performance, 30 arrays were coated with polycrystalline HgI_2 over a period of 4 years—23 with PVD and 7 with PIB. Among

Table 2. Summary of information related to the details of the polycrystalline HgI_2 detector for each of the prototype arrays evaluated in this study. Note that the second last column gives the thickness of each PVD and PIB coating.

Prototype code	Deposition method	Array design	Deposition date	Thickness (μm)	Barrier type
PVD#1	PVD	ND10	12/02	300	D
PVD #2	PVD	ND10	12/02	300	A
PVD #3	PVD	ND10	04/03	290	A
PVD #4	PVD	ND10	05/03	210	A
PVD #5	PVD	ND10	06/03	265	D
PVD #6	PVD	ND10	07/03	280	D
PVD #7	PVD	ND10	08/03	300	D1
PVD #8	PVD	ND10	08/03	300	D2
PVD #9	PVD	ND10	08/03	300	D1
PVD #10	PVD	ND10	11/03	230	D2.1
PVD #11	PVD	ND10	11/03	225	D2
PVD #12	PVD	ND10	01/04	280	D2.2
PVD #13	PVD	ND10	01/04	285	D2.3
PVD #14	PVD	ND10	06/04	230	D2.3
PVD #15	PVD	MD88	09/05	290	D2.4
PVD #16	PVD	MD88	01/06	280	D2.4
PIB#1	PIB	ND10	06/04	460	D2
PIB#2	PIB	ND10	10/04	615	D2
PIB#3	PIB	MD88	09/05	620	D2
PIB#4	PIB	MD88	01/06	635	D2

these, a total of 20 prototype arrays exhibited sufficiently good performance to allow detailed evaluation. Information about the evaluated prototypes is summarized in table 2, ordered by the date when the HgI_2 depositions were performed. The photoconductor thicknesses range from 210 to 300 μm for PVD, and from 460 to 635 μm for PIB. Given packing densities of $\sim$90% and 50% for PVD and PIB, respectively, the amount of HgI_2 per unit area deposited on the prototypes corresponds to roughly the same range for the two forms of the material. Finally, the parameters chosen for creating the PVD or PIB detector for each prototype (deposition conditions, photoconductor thickness, barrier type etc) were based on the goal of simultaneously minimizing W_{EFF} and dark current, and maximizing MTF—with parameters chosen based on the performance of previously evaluated prototypes.

2.5. Data acquisition

The prototype arrays were wirebonded to custom-designed, multi-layer printed circuit motherboards, and the motherboards were attached to a previously developed, electronic acquisition system (Huang *et al* 1999) incorporating a custom-designed, low-noise, 32-channel preamplifier-multiplexer chip with a large signal capacity (Yarema *et al* 2000). Readout of all, or of any contiguous part of a prototype by the acquisition system results in a single data frame. The system was operated so as to produce a continuous stream of data frames—with the time from the start of one frame to the start of the next frame referred to as the frame time, T_F. Unless otherwise specified, most data were acquired from the entire prototype at a T_F of $\sim$0.3 s. Data frames acquired in the absence or presence of radiation are referred to as dark and image frames, respectively. Both dark frames and image frames were obtained in an

optically dark environment where the temperature was regulated at ~23 °C. The acquisition system was turned on well in advance of any measurements to allow the electronics and the prototype to reach thermal equilibrium.

Data were acquired both radiographically and fluoroscopically. In radiographic and pulsed fluoroscopic operation, the delivery of a single x-ray pulse was synchronized with the readout of a prototype (Antonuk *et al* 1997). Finally, in continuous fluoroscopic mode, the prototype was read out repeatedly during the delivery of a long, continuous irradiation, without any synchronization. For all modes of operation (unless otherwise indicated), the resulting data set consists of a sequence of dark frames followed by one or more image frames.

X-ray measurements were performed at 72 kVp using a Dunlee PX1415 x-ray tube, operated with a Picker 380 high-frequency generator. 20 mm of aluminum filtration was used in addition to an inherent filtration of 3.2 mm of aluminum, resulting in a half value layer of 7 mm aluminum. The distance from the x-ray source to the prototype surface (source-to-detector distance) was 100 cm, unless otherwise specified. The exposure for each image frame was measured by means of a calibrated ion chamber (Keithley 96035) connected to a Keithley 35050A dosimeter. The ion chamber was located next to the prototype at the same source-to-detector distance.

2.6. Performance evaluation methods

The techniques used to measure the properties reported in this paper are described below. For a given prototype array, results are reported for a single value of electric field across the photoconductor—a value based on the x-ray signal response and dark current of the prototype, as described in section 3.1.

2.6.1. Dark signal properties. Readout of a prototype array in the absence of radiation provides a means of examining the dark signal behavior of the pixels—where the observed pixel signal results from a combination of dark current in the photoconductor, leakage current in the pixel TFT and a fixed offset from the acquisition electronics. The slope of pixel dark signal plotted as a function of frame time, T_F, provides a measure of pixel dark current (Antonuk *et al* 1997). At sufficiently large values of T_F (typically beyond a few seconds), the dark current is dominated by the contribution from the photoconductor. Thus, photoconductor dark current was examined via measurements of pixel dark signal for T_F values up to 10 s. In addition, pixel dark signal stability was examined by reading out dark signal over a period of 30 min.

2.6.2. Charge trapping and lag. The amount of charge trapping in, and charge release (i.e., lag) from the detectors was examined through measurement of consecutive data frames acquired in pulsed fluoroscopic mode, following a previously developed technique (Antonuk *et al* 1992b, 1997). Further details are given in section 3.

2.6.3. Pixel response and linearity. The pixel response to radiation as a function of exposure was examined through radiographic and continuous fluoroscopic measurements. In order to extend these pixel signal measurements as close to saturation as possible, the source-to-detector distance was decreased to 54 cm. This was sufficient to achieve saturation in radiographic mode. However, in continuous fluoroscopic mode, the x-ray unit limited the tube current so that saturation was not possible. This was partially compensated for by increasing T_F to 1.6 s for these particular measurements, resulting in a minimum and maximum exposure per frame

(limited by the available range of tube current) of 0.5 and 5 mR, respectively. In radiographic mode, measurements were performed for exposures per frame ranging from ~0.2 to 20 mR. An analysis of the shape of the resulting pixel response data was used to quantify the degree of linearity, following a previously reported method (Antonuk *et al* 1997).

2.6.4. Uniformity of pixel signal response. The degree to which pixel x-ray signal varied from pixel to pixel on a given prototype array was quantified through analyses of data from image frames acquired in radiographic mode. For each prototype, a region of interest (ROI) was defined consisting of a block of thousands of pixels. These blocks were largely free of non-functioning pixels, and their pixel properties were representative of properly functioning parts of the prototype. The maximum dimensions of each ROI was sufficiently small that spatial variations in x-ray fluence across the ROIs was less than 1%. Image frames were acquired at four exposures, ranging from ~0.04 to 0.4 mR per frame. At each exposure, non-uniformity in pixel signal response was determined by making a histogram of the pixel signal data, and then calculating the ratio of the standard deviation to the mean of the resulting distribution.

2.6.5. X-ray sensitivity and W_{EFF}. X-ray sensitivity was obtained using the mean values of the distribution of the pixel x-ray signal data acquired for the pixel signal uniformity study. The range of exposures for which data were acquired corresponded to the first ~20% of pixel signal capacity—a region where pixel signal was found to be highly linear with increasing exposure. For each prototype array, sensitivity was determined from the slope of these mean signal values versus exposure. The effective work function was then determined from the average absorbed x-ray energy per unit exposure divided by x-ray sensitivity expressed in units of electrons collected per pixel per unit exposure. The energy absorbed in the photoconductor material was calculated from Monte Carlo simulations, using the EGS4 code (Nelson and Rogers 1989), the RZ_PHS user code (Jaffray *et al* 1995) and an x-ray spectrum corresponding to an appropriate peak energy and beam filtration obtained from (Boone and Seibert 1997).

2.6.6. Presampled modulation transfer function (MTF). The one-dimensional presampled MTF of the prototype arrays was determined using the angled slit technique (Fujita *et al* 1992), employing a 15 cm long slit formed by a pair of 15 × 10 × 0.6 cm^3 tungsten slabs separated by 10 μm shims. The x-ray field was projected through the slit on the prototype at a small angle (~1°) relative to the direction of the data address lines. The oversampled line spread function (LSF) was acquired from the average of images of the slit, and the presampled MTF was determined from the Fourier transform of the LSF.

2.6.7. Noise power spectra (NPS). The general methodology used to obtain NPS has been described previously (Jee *et al* 2003) and details specific to the present measurements are briefly summarized below. One-dimensional empirical NPS were determined from images taken in continuous fluoroscopic mode, at a T_F of 84.7 ms, for exposures ranging from 3.4 to 20 μR, and at a source-to-detector distance of 135 cm. The analysis of the image data employed the synthesized slit technique. Each slit consists of 250 × 50 pixels, with the long dimension oriented along the gate line direction. For each image, a region of interest consisting of a block of 250 × 250 pixels, containing a minimal number of pixel and line defects, was chosen. The bad lines and defective pixels (representing less than 0.3% of the total number of pixels) were corrected by a median filter. Each slit was summed in the data line direction to yield a realization of one dimensional data, followed by the applications of a

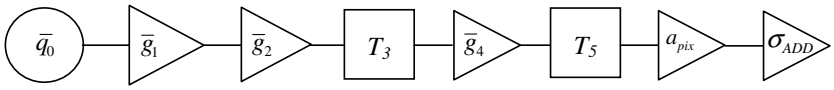

Figure 2. Block diagram representing the various stages in the serial cascaded systems analysis performed in this paper for prototype PVD#4. The x-ray spectrum (Boone and Seibert 1997) used in the calculations corresponds to that used in our measurements and is characterized by a fluence of $\bar{q}_0 = 262\,410$ x-rays mm^{-2} mR^{-1}. The HgI_2 photoconductor is described by a quantum efficiency $\bar{g}_1 = 0.643$ with a variance of 0.229. It is also described by a photoconductive gain represented by $\bar{g}_2 = 11\,246$ (mean number of electron-hole pairs generated in the photoconductor per interacting x ray) with a variance of 9.86×10^6—as determined via EGS4 Monte Carlo simulations (El-Mohri *et al* 2007) assuming a thickness of 210 μm for HgI_2, a density of 5.72 g cm^{-3} and an internal ionization energy of 4.2 eV (Schieber *et al* 1997, Alexiev *et al* 2004). The stochastic spatial spreading is characterized by T_3 obtained from the empirically determined MTF divided by the sinc function for a square pixel aperture of 127 μm. The gain $\bar{g}_4 = 0.392$ with a variance of 0.238 corresponds to the collection efficiency of charges created in the photoconductor. The value of $\bar{g}_4$ was obtained by fitting the calculated x-ray sensitivity to the empirically determined value, with $\bar{g}_4$ taken as a free parameter. The array pixels are characterized by a spatial spreading represented by the aforementioned sinc function, T_5, and an additional stage (labeled a_{pix}) representing the sampling of the signal. The additive noise of the electronic acquisition system is characterized by σ_{ADD}, which was empirically determined from dark NPS measurements to be ~2000 e (rms). Note that, for simplicity, k-fluorescent interactions have not been separated as a parallel branch in the model since their effect on the MTF, as determined from Monte Carlo simulations that include such interactions, was found to be negligible.

Hanning window and a Fourier transform, resulting in a one-dimensional NPS. The empirical NPS values were determined from the average of 300 non-overlapping realizations, both in the presence (x-ray NPS) and absence (dark NPS) of x-ray irradiation. Since the data were taken in continuous fluoroscopic mode, signal from one image frame may carry over into subsequent frames, resulting in a reduced NPS due to averaging. For this reason, a lag correction was applied to the measured x-ray NPS (Granfors and Aufrichtig 2000).

2.6.8. DQE determination. DQE performance was empirically determined using the equation (Shaw 1963, Cunningham and Shaw 1999)

$$\mathrm{DQE} = \frac{\bar{d}^2 \times \mathrm{MTF}^2}{\bar{q}_0 \times \mathrm{NPS}}, \tag{1}$$

where $\bar{d}$ is the average pixel signal, MTF is the presampled MTF, $\bar{q}_0$ is the mean fluence (i.e., number of incident x-rays per unit area), and NPS is the empirically determined noise power spectrum of the image frames.

For purposes of comparison, DQE was also calculated using cascaded systems analysis, which has been widely employed to successfully describe the DQE performance of AMFPIs (Cunningham *et al* 1994, El-Mohri *et al* 2001, Zhao *et al* 2003). In this formalism, an imaging system is considered to consist of a series of stages, where each stage represents a physical process characterized by a gain ($\bar{g}_i$), with a corresponding variance $\left(\sigma_{gi}^2\right)$, or by a spatial spreading of image quanta (represented by an MTF, T_i). A schematic illustration of the various stages used in the present analysis is shown in figure 2.

3. Results

Results obtained from the 20 prototype arrays whose signal behavior was sufficiently good to allow detailed evaluations are summarized in this section. For some properties (dark current,

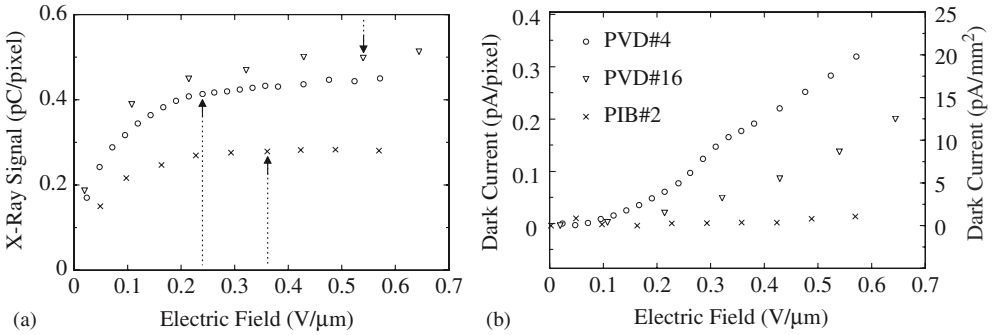

Figure 3. (a) Pixel x-ray signal and (b) pixel dark current as a function of electric field up to 0.7 V μm^{-1}. The results correspond to averages over more than a thousand pixels in a largely defect-free region for prototypes PVD#4, PVD#16 and PIB#2. For each prototype, the dashed vertical arrow in (a) corresponds to the selected electric field strength at which properties for this array were measured. Note that the right-hand side scale in (b) corresponds to normalization of the dark current to unit photoconductor area, based on a 127 × 127 μm^2 pixel area.

dark signal drift, lag, linearity, radiographic sensitivity and the corresponding W_{EFF}, and uniformity of pixel signal response), unambiguous and reproducible results, free of anomalous signal behaviors, were obtained from most or all of the prototypes and are reported. For other properties (charge trapping and MTF), reportable results could be obtained only from some of the prototypes. The results are presented in the form of tables or charts. In addition, detailed results are shown in graphical form for a few selected prototypes that exhibited either typical or noteworthy behaviors. Detailed results are also shown for PVD#4 whose properties were, among those observed across all of the prototypes, best suited to allow determination of DQE. In addition, a cascaded system analysis, performed to allow comparison of theoretical DQE performance against the results observed from this prototype, is reported. Finally, note that for all reported results derived from image frames, the pixel dark signal contribution (independently determined from one or more dark frames) has been subtracted.

3.1. Selection of electric field strength

Figure 3(a) illustrates the dependence of the magnitude of the x-ray pixel signal on the electric field strength across the photoconductor for three prototype arrays. For each prototype, the x-ray signal increases with field strength until asymptotically approaching a plateau of maximum value. The field strength at which the plateau was reached varied from prototype to prototype. Given that the motivation for the development of the polycrystalline HgI_2 material is to significantly increase the pixel x-ray signal, this would encourage the use of a field strength sufficiently high so as to operate in the region of the plateau. However, dark current exhibits a strong, nonlinear dependence on electric field strength. This is apparent in figure 3(b) for the two PVD prototypes, but less so for the PIB prototype which demonstrated considerably smaller dark current. These behaviors are similar to those reported in earlier studies involving simple polycrystalline HgI_2 detectors (Su *et al* 2005). Since higher dark current more rapidly consumes pixel signal capacity, as well as increases shot noise, the selection of electric field strength therefore generally involves a tradeoff between high x-ray signal and low dark current. In the present study, the value of electric field strength was generally chosen based on consideration of this tradeoff (For PVD#6, PVD#9 and PVD#14, the field strengths were further limited so as to not draw extremely high currents from the high voltage power supply

Table 3. Summary of electric field strengths used in this study, along with the corresponding pixel x-ray signal size, expressed in per cent of the maximum extracted signal. In addition, results are given for dark current, drift in pixel dark signal. The dark current and drift results correspond to averages over ∼10 properly functioning pixels. Note that the dark current results are reported both in terms of the magnitude per pixel as well as per unit area of photoconductor.

Prototype code	Electric field strength	Signal extraction	Photoconductor dark current		Drift in pixel signal over 30 min
	V μm^{-1}	%	pA/pixel	pA mm^{-2}	fC/pixel
PVD#1	0.53	95	0.19	12	10
PVD#2	0.40	95	0.21	13	21
PVD#3	0.24	100	0.37	23	2.6
PVD#4	0.24	91	0.11	6.8	1.5
PVD#5	0.26	98	0.19	12	11
PVD#6	0.43	81	0.12	7.4	2.3
PVD#7	0.33	91	0.19	12	4.0
PVD#8	0.17	90	0.19	12	1.7
PVD#9	0.10	84	0.077	4.8	0.97
PVD#10	0.35	93	0.17	11	9.8
PVD#11	0.27	95	0.11	6.8	4.2
PVD#12	0.25	96	0.054	3.3	0.97
PVD#13	0.18	93	0.013	0.81	1.6
PVD#14	0.17	89	0.15	9.3	7.8
PVD#15	0.59	96	0.094	5.8	2.8
PVD#16	0.54	93	0.12	7.6	2.5
PIB#1	0.35	96	0.0076	0.47	0.62
PIB#2	0.36	99	0.0016	0.10	0.79
PIB#3	0.50	98	0.023	1.4	0.62
PIB#4	0.43	99	0.028	1.7	0.79

due to damaged or otherwise abnormally-performing parts of the prototype.) The resulting field strengths, which are listed in table 3, range from 0.10 to 0.54 V μm^{-1} and 0.35 to 0.50 V μm^{-1} for the PVD and PIB prototypes, respectively. The corresponding percentage of pixel signal extraction at the field strengths are also given in the table and range from 81% to 100%. Therefore, the properties reported in this paper were obtained under conditions where each prototype was operated so as to allow extraction of the maximum x-ray signal, limited by dark current considerations.

3.2. Dark current and dark signal drift

Dark current for each prototype array, measured under conditions where the contribution of the photoconductor is dominant, is listed in table 3. The results are expressed both in terms of dark current per pixel as well as dark current per unit area of photoconductor (the latter obtained from the former through division by the pixel area). The dark current was found to range from ∼0.81 to 23 pA mm^{-2} and ∼0.10 to 1.7 pA mm^{-2} for the PVD and PIB prototypes, respectively. In general, the dark current was found to be considerably smaller for the PIB prototypes. Moreover, among the PVD prototypes, the two MD88 arrays (PVD#15 and PVD#16) demonstrated significantly lower dark current than the ND10 arrays at comparable electric field strengths, suggesting that a higher degree of uniformity of the array surface may reduce dark current. Note that one PVD prototype (PVD#13) and two PIB prototypes (PIB#1 and PIB#2) demonstrated dark current levels less than 1 pA mm^{-2}—corresponding

to a level of performance routinely achieved by commercial direct and indirect detection AMFPIs. In addition, the results of pixel dark signal drift, over a period of 30 min, are listed for each prototype in table 3. The dark drift ranged from ∼0.97 to 21 fC/pixel and ∼0.62 to 0.79 fC/pixel for the PVD and PIB prototypes, respectively. In comparison, indirect detection arrays normally exhibit extremely little drift over much longer periods.

It is also interesting to note that, for some prototypes, when an electric field was first applied, an abnormally high current was drawn from the high voltage power supply, even at relatively low field strengths (i.e. up to several hundred microamperes at less than 0.5 V μm^{-1}). However, after such prototypes were left under bias for a few hours, the current would gradually reduce to more reasonable levels (less than a few microamperes) and remain relatively low thereafter. Of the various mechanisms that could be responsible for this behavior, one possibility is unintended metallic pathways, created during deposition of the top electrode, that short this electrode to underlying array elements, most likely pixel collection electrodes. Such shorts would generate large currents upon the initial application of bias, until electrochemical reactions (or electromigration) eventually eliminate the shorted pathways. Another possibility is ionic conduction caused by migration of Hg^{2+} and I^- ions which could lead to large currents over many hours, until the available unbonded ions have migrated.

3.3. Charge trapping, lag and polarization

The effects of charge trapping, charge release (i.e. lag) and polarization are illustrated in figure 4, where pixel signal data sets acquired from consecutive data frames, for three prototype arrays operated in pulsed fluoroscopic mode, are presented. Each data set corresponds to the signals from a single, representative pixel over initial 50 dark frames, followed by at least 70 image frames, followed by final 200, or more, dark frames. For each image frame, the radiation was delivered in a brief pulse at the beginning of the frame, followed by the readout of the prototype. The exposure per frame was chosen so as to result in signal levels of 15%, or less, of pixel saturation. In figures 4(a) and (b), pixel x-ray signal response demonstrates a relatively rapid increase from the first image frame (frame #50), reaching an asymptotic signal level in later image frames, and then quickly diminishing following the last image frame—a behavior closely paralleling that observed from a-Si:H photodiodes in indirect detection array studies (Antonuk *et al* 1992a, 1997) As in that case, the behavior of pixel x-ray signal response during the first few image frames is attributed to a temporary loss of signal due to charge trapping in electronic states in the gap between the conductive and valance bands of the photoconductor. The asymptotic behavior in later image frames is due to establishment of an equilibrium between charge trapping and charge release in the photoconductor. The declining pixel signal after the last image frame is due to the gradual release of trapped charge. The relative amount of charge lost to trapping, Q_T, was quantified using the expression

$$Q_T = (Q_{EQ} - Q_F)/Q_{EQ}, \tag{2}$$

where Q_F is the pixel x-ray signal for the first image frame, and Q_{EQ} is the average pixel x-ray signal of the last five image frames (where equilibrium has been established)—as illustrated in figure 4(a). For the data shown for PVD#1 and PVD#4, charge trapping was determined to be ∼19% and ∼11%, respectively. Charge trapping results obtained from most of the prototypes are summarized in table 4. The results are generally in excess of 20%, indicating high levels of charge trapping compared to levels as low as ∼5% observed for indirect detection arrays (Antonuk *et al* 1997).

More complicated charge trapping behaviors are illustrated in figure 4(c). In this case, while the pixel demonstrated typical charge trapping behavior at very low pixel signal levels

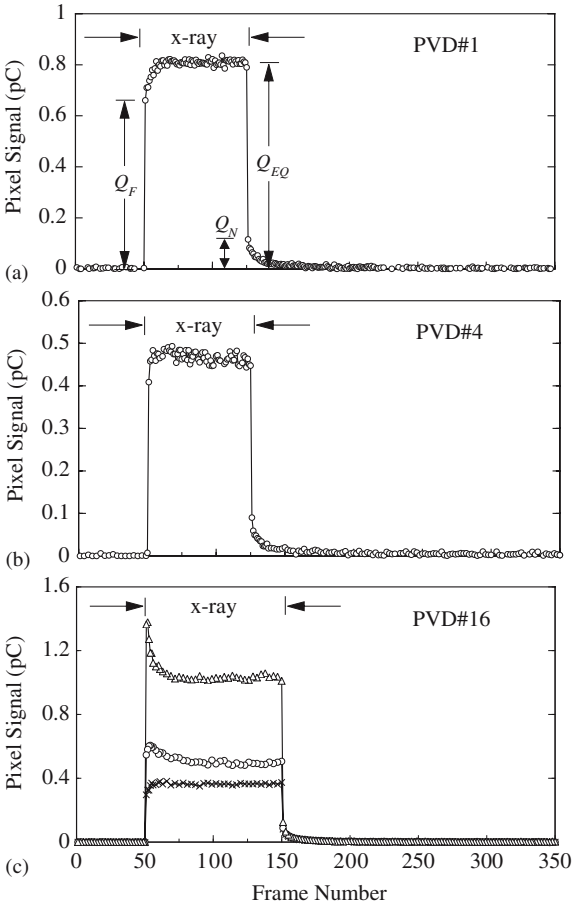

Figure 4. Data from individual array pixels illustrating charge trapping, charge release (i.e. lag) and polarization effects. Pixel signal data measured initially in the absence, then the presence, and finally the absence of radiation are plotted as a function of consecutive frame number. Data are shown for prototypes (a) PVD#1 at an equilibrium signal level of ∼10% of pixel saturation; (b) PVD#4 at an equilibrium signal level of ∼8%; and (c) PVD#16 at equilibrium signal levels of ∼3%, 6% and 15% (indicated by cross, circle and triangle symbols, respectively).

($Q_T = 21\%$ at ∼3% of pixel saturation), at higher exposures the pixel x-ray signal actually declined following the initial image frame, and the amount of decline became larger with increasing pixel signal size. It is suspected that this behavior is a result of charge being trapped by a different mechanism for somewhat longer periods of time somewhere in the structure of the detector. The most likely mechanism is the trapping of charge at the interface between the barrier layer and the photoconductor. As the trapped charge accumulates at this interface, a voltage drop across the barrier would increase, resulting in a reduction in the electric field across the photoconductor, which diminishes the efficiency of charge transport and collection. Such an effect may be considered as a form of polarization, as described by previous investigators (Schieber *et al* 2000). Such polarization effects were generally observed for both the PIB and PVD prototypes at higher exposures. However, the lowest exposure at which a given prototype would first exhibit polarization varied widely among the prototypes.

Table 4. Charge trapping and first frame lag results measured from the prototype arrays. These results are expressed as a percentage of the pixel x-ray signal, Q_{EQ}. The second column indicates the pixel signal level, expressed in terms of percentage of pixel saturation, at which the measurements were performed. For a given prototype, the reported trapping and lag values correspond to the range of results measured from properly functioning pixels. Results are not reported for prototypes exhibiting anomalous signal behaviors.

Prototype code	Pixel signal size (% of saturation)	Q_T (%)	Q_{LAG} (%)
PVD#1	10	20–30	12–16
PVD#2	15	4–38	10–13
PVD#3	7	6–47	7–16
PVD#4	8	0.3–39	11–19
PVD#5	12	29–38	16–27
PVD#6	3	19–55	13–24
PVD#7	2	19–43	13–19
PVD#8	2	21–38	15–25
PVD#9	1	24–46	5–20
PVD#10	2	14–43	9–21
PVD#11	2	–	12–16
PVD#12	2	5–56	21–31
PVD#13	6	–	25–31
PVD#14	3	30–45	13–19
PVD#15	3	–	21–33
PVD#16	1	24–40	15–25
PIB#1	4	47–76	37–63
PIB#2	1	6–36	16–39
PIB#3	2	–	16–18
PIB#4	1	23–48	17–29

Finally, the relative amount of first frame lag, Q_{LAG}, was quantified using the expression

$$Q_{\mathrm{LAG}} = Q_N / Q_{\mathrm{EQ}}, \tag{3}$$

where Q_N is the pixel signal for the first dark frame following the last image frame, as illustrated in figure 4(a). Based on the data shown in figure 4, Q_{LAG} is ∼14% and ∼20% for PVD#1 and PVD#4, respectively. For PVD#16, Q_{LAG} is ∼18%, 12% and 11% for signal levels of 3%, 6% and 15% of pixel saturation, respectively. The lag values measured from the prototypes are given in table 4 and range from ∼5% to 63%—generally consistent with the high levels of charge trapping noted above. These lag values are significantly larger than levels as low as ∼2% observed for indirect detection arrays (Antonuk *et al* 1992b, 1997).

3.4. Pixel response and linearity

Pixel x-ray signal data, typical of that observed from the various prototype arrays, are plotted as a function of exposure for PVD#4 and PVD#15 in figures 5(a) and (b), respectively. In radiographic mode, the pixel response initially exhibits relatively linear behavior before beginning to depart from linearity. As exposure increases, the departure from linearity progressively increases until the pixel saturates (or approaches saturation).

In fluoroscopic mode, the pixel response shows an earlier, and stronger departure from linearity with increasing exposure. (Restrictions imposed by the x-ray source limited the maximum exposure possible for this mode—as detailed in section 2.6.3.) Given that the fluoroscopic data were taken under conditions where charge trapping and charge release are

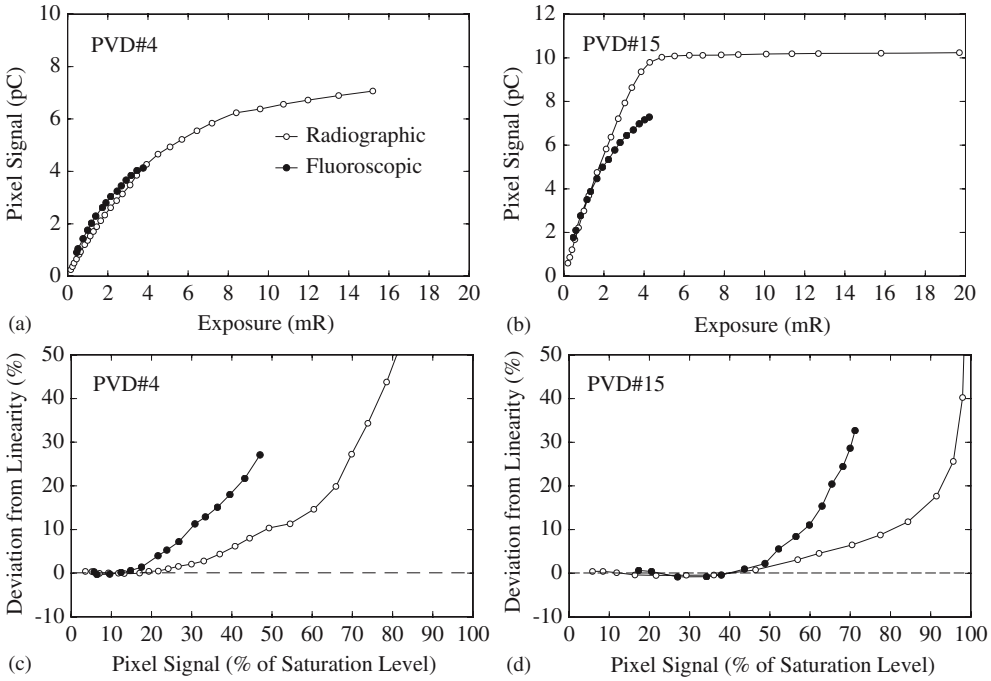

Figure 5. X-ray pixel signal response averaged over a large number of properly functioning pixels, plotted as a function of exposure, for prototypes (a) PVD#4 and (b) PVD#15. The degree of nonlinearity in this x-ray response data is plotted in (c) for PVD#4 and (d) for PVD#15.

in equilibrium (which tends to make the pixel signal response considerably more linear for fluoroscopic mode than for radiographic mode in indirect detection arrays) (Antonuk *et al* 1997), the behavior exhibited in the figures is somewhat surprising. It is suspected that this comparatively high degree of nonlinearity in fluoroscopic mode is a result of the polarization phenomenon noted in section 3.3. In this interpretation, the effect of polarization will be to progressively suppress fluoroscopic x-ray signal as exposure increases. (For example, as observed in figure 4(c) where polarization effects are pronounced at higher exposures, the fluoroscopic signal, which corresponds to the equilibrium level, is lower than the radiographic signal (first image frame).) Thus, while one would still expect the pixel signal to saturate at the same level for radiographic and fluoroscopic modes, it will require a higher exposure to reach saturation in fluoroscopic mode.

Quantification of the degree of linearity of each set of pixel response data in figures 5(a) and (b) was carried out as follows. A linear fit of the data up to ∼20% of pixel saturation was performed and the difference between the results of the fit and the measured pixel signal, expressed as a percentage of the saturation signal, was calculated. (In this analysis, the pixel signal level at saturation for fluoroscopic mode is assumed to be the same as for the corresponding radiographic mode results.) The results of this analysis, appearing in figures 5(c) and (d), are plotted as a function of pixel signal size, in units of percent of pixel saturation. In radiographic mode, the signal size at which the degree of non-linearity exceeds 1% (one measure of good linearity) (Antonuk *et al* 1997) is at ∼24% and 48% for PVD#4 and PVD#15, respectively. For fluoroscopic mode, nonlinearity exceeds 1% at lower signal levels, ∼16% and 44%, respectively. Figure 6 summarizes, for radiographic mode, the signal

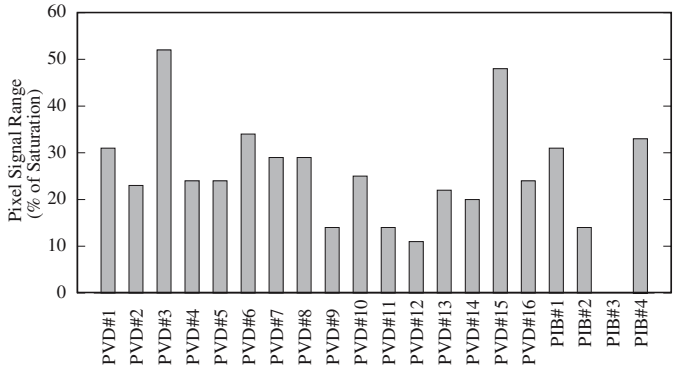

Figure 6. Pixel response linearity measured in radiographic mode, presented in the form of a bar chart. For each prototype, linearity is reported in terms of the pixel signal range (expressed in units of percent of pixel signal saturation) over which the degree of nonlinearity is less than 1%.

size at which nonlinearity exceeds 1% for most of the prototypes and the results are seen to range from 11% to 52%. (The quality of the majority of the fluoroscopic data was insufficient to provide meaningful results.) By comparison, indirect detection arrays commonly exhibit good linearity up to at least 65% for radiographic mode, and ∼75% or higher for fluoroscopic mode (Antonuk *et al* 1997).

3.5. Non-uniformity of pixel signal response

Histograms of pixel x-ray signal data, acquired at four exposure levels for several prototype arrays, are shown in figure 7. The results shown on the left (7 (a), (c), (e) and (g)) correspond to pixel data corrected only for dark signal. The resulting distributions have Gaussian-like shapes. The graphs on the right (7(b), (d), (f) and (h)) show distributions for the same data after application of a gain correction. Ideally, for a photoconductor, the application of this correction would reduce the width of each distribution to a level consistent with the x-ray statistics of the corresponding exposure. For purposes of comparison, the Gaussian distribution corresponding to the x-ray statistics for each exposure for each prototype is plotted as a solid line on the right-hand side graphs. In addition, for each histogram shown in figure 7, the data were fit by a Gaussian curve (not shown). The ratio of the resulting standard deviation to the centroid of each fit is a measure of the degree of non-uniformity of the pixel x-ray signal response. The results of this analysis are discussed below, and those results corresponding to the lowest (∼0.058 to 0.136 mR) and to the highest (∼0.206 to 0.380 mR) exposure levels are illustrated for all of the prototypes in figures 8(a) and (b), respectively. Figure 8 also illustrates the non-uniformity corresponding to x-ray statistics.

A variety of interesting behaviors and trends are apparent in figures 7 and 8. There is considerable variation in non-uniformity before gain correction from prototype to prototype for a given exposure level. For all PVD prototypes except PVD#6, the degree of non-uniformity always decreases with increasing exposure. This trend is in line with the behavior to be expected based on x-ray statistics alone. However, for the PIB prototypes, no such trends were evident in the data. For the PVD prototypes, the non-uniformity ranged from ∼11% to 50% and ∼7% to 31% for the lowest and highest exposure levels respectively. For the PIB prototypes, the non-uniformity was ∼11% for the best prototype and ∼37% for the worst prototype at highest exposure levels.

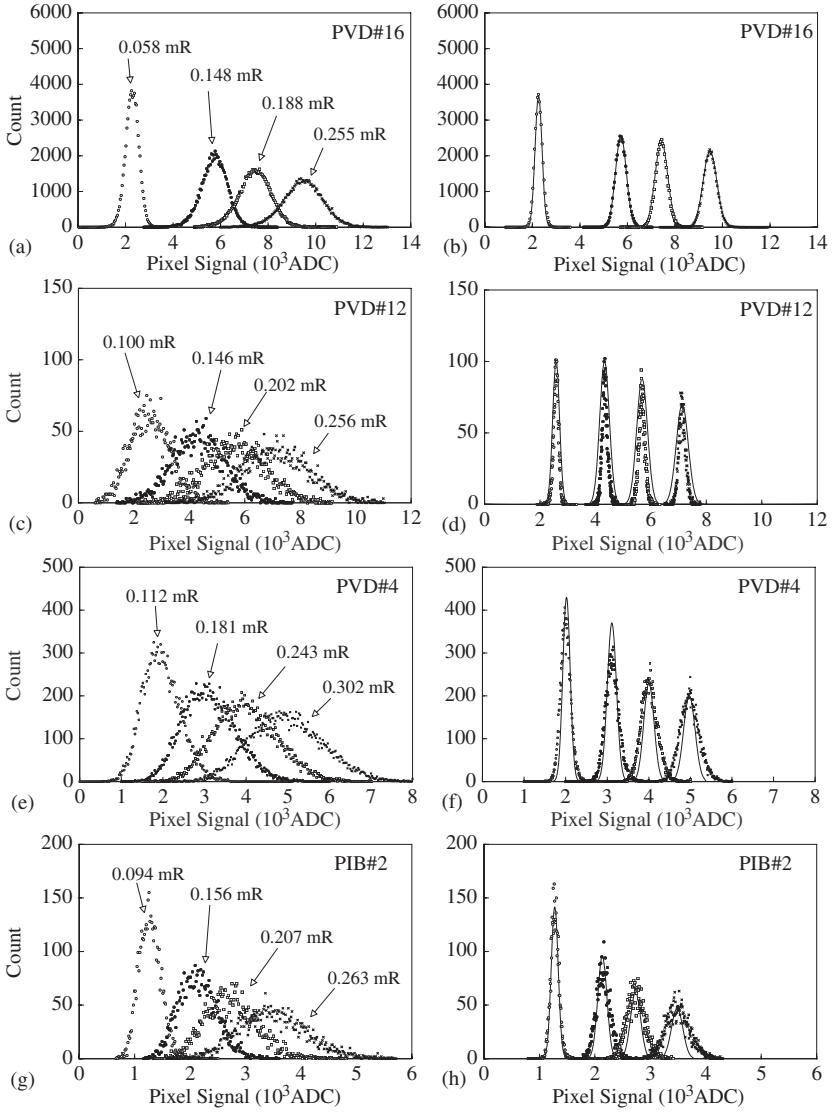

Figure 7. Histograms of pixel x-ray signal for prototypes (a), (b) PVD#16, (c), (d) PVD#12, (e), (f) PVD#4 and (g), (h) PIB#2. Results are shown for four exposures. The graphs on the left correspond to pixel data which have been corrected only by a dark signal subtraction. The graphs on the right correspond to the same data, after the application of a gain correction which primarily accounts for pixel-to-pixel variation in x-ray signal response (Antonuk *et al* 1992a). This correction is based on five image frames acquired independently under the same conditions. The solid lines imposed on these graphs represent histograms to be expected based on x-ray statistics.

For a given prototype, the degree of non-uniformity, before gain correction, is considerably larger than what would be expected based on x-ray statistics alone, ranging from ∼2.4 to 11 times, and ∼4.5 to 14 times larger at the highest exposure level for PVD and PIB, respectively. This is considerably greater than what could be accounted for by the estimated 10% variation in HgI_2 thickness across a given prototype. Interestingly, careful microscopic examination of representative samples of the PVD and PIB material revealed no evidence of

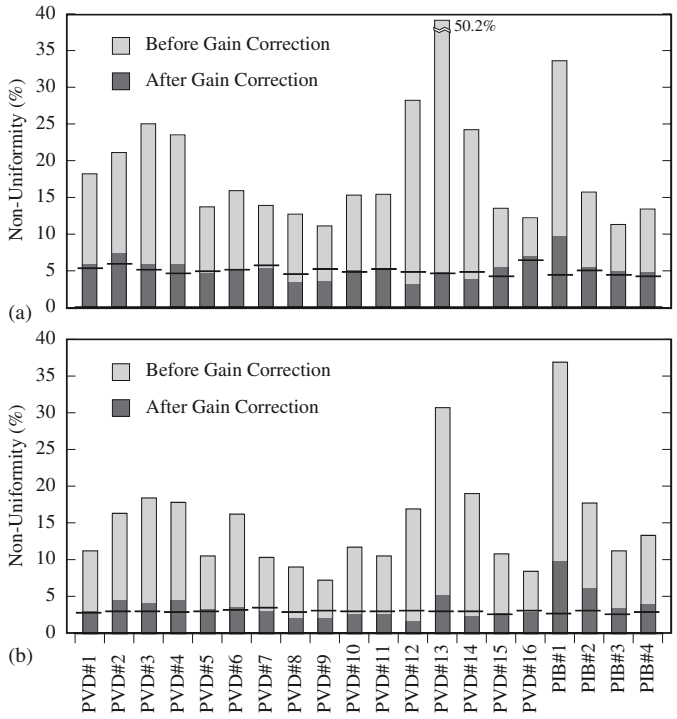

Figure 8. Summary of the non-uniformity in x-ray signal response measured from a ROI of several thousand pixels for each prototype. Results are shown in the form of a bar chart for (a) the lowest exposures, ranging from 0.058 to 0.136 mR, and (b) the highest exposures, ranging from 0.206 to 0.380 mR. In each chart, for a given array, the non-uniformity before and after the application of a gain correction to the data is indicated by the top of the lighter and darker shaded portion of the bar, respectively. In addition, the non-uniformity to be expected, based only on considerations of the x-ray statistics of the image frame from which the data for this prototype were obtained, is indicated by a horizontal line across the corresponding bar.

any non-uniformities in photoconductor thickness or structure that are sufficient to explain the observed magnitude of pixel-to-pixel signal non-uniformities.

The application of gain correction reduces the degree of non-uniformity to ∼0.57 to 1.8 times, and ∼1.4 to 3.8 times that of x-ray statistics at the highest exposure level for PVD and PIB, respectively—demonstrating considerable variation between prototypes. In some cases, such as for PVD#16 (figure 7(b)), there is good agreement. In other cases, such as for PVD#12 (figure 7(d)), the corrected data are actually more uniform than x-ray statistics would predict. This latter behavior suggests the existence of a small degree of charge sharing between adjacent pixels—which would increase the number of x-ray interactions effectively sampled by each pixel and result in small decreases in the width of the distribution. Finally, in yet other cases, such as for PVD#4 (figure 7(f)), and all the PIB prototypes, the corrected data are less uniform than predicted by x-ray statistics. Such behavior must result from at least some degree of anomalous temporal variation in the x-ray signal response from pixel to pixel.

3.6. X-ray sensitivity and W_{EFF}

X-ray sensitivity results obtained from the prototype arrays are shown in figure 9. The results, determined using data from the uniformity study, range from 1.4 to 3.3 and 0.76 to

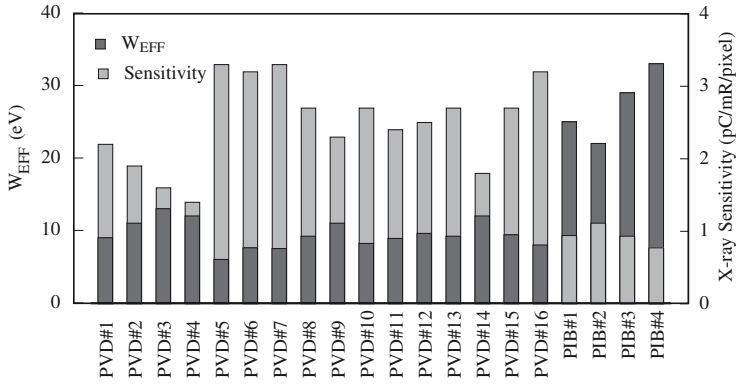

Figure 9. Pixel x-ray signal sensitivity measured in radiographic mode and the corresponding W_{EFF} obtained from blocks of hundreds to thousands of pixels in largely defect-free regions of the prototypes, presented in the form of a bar chart. For a given array, the W_{EFF} and the corresponding sensitivity are indicated by the top of the darker and lighter shaded portions of the bar, corresponding to the left and right scales, respectively.

1.1 pC/mR/pixel for the PVD and PIB prototypes, respectively. W_{EFF} values for the prototypes, determined from a combination of measured sensitivity results and energy deposition values obtained from Monte Carlo simulations, are also presented in figure 9. These results range from 6.0 to 13 eV for the PVD prototypes—lower than values of 22 to 33 eV determined for the PIB prototypes. The lowest W_{EFF} observed, 6.0 eV is close to the theoretical minimum of ∼4.2 eV corresponding to the property of the single crystal form of HgI_2 (Schieber *et al* 1997, Alexiev *et al* 2004). By comparison, an earlier study performed with simple, non-pixelated film detectors, fabricated in the same manner and measured under the same irradiation conditions as in the present study, found W_{EFF} values as low as ∼7 and 9 eV for PVD and PIB detectors, respectively (Su *et al* 2005). The present PVD prototype results represent a substantial improvement over the W_{EFF} values for Gd_2O_2S:Tb, CsI:Tl and a-Se, which are on the order of ∼25, 24 and 50 eV, respectively (Rieppo and Rowlands 1997). Moreover, these low W_{EFF} values were achieved at substantially lower electric fields (less than 0.6 V μm^{-1}) than the ∼10 V μm^{-1} required for a-Se (Zhao and Rowlands 1995).

3.7. MTF

Monte Carlo simulation of x-ray energy deposition in HgI_2 indicates that there is very limited x-ray scattering at the beam energy of this study. Thus, if the charge deposited by the x-rays is assumed to directly traverse the photoconductor, then the MTF of the array–detector combination should be very close to the theoretical limit defined by the sinc function corresponding to the pixel pitch of the array. MTF curves measured from four prototype arrays are shown in figure 10. For purposes of comparison, MTFs derived from published results for direct and indirect detection AMFPIs using a-Se and CsI:Tl detectors, respectively, are also shown in the figure. In addition, the MTF at 2 lp mm^{-1} and 4 lp mm^{-1} for most of the prototypes is summarized in figure 11.

The MTF results are observed to vary widely among the prototypes with no clear correlation with detector thickness—for example, prototype PVD#12 and PVD#16 have a similar thickness but significantly different MTF values. Several prototypes (e.g., PVD#2, PVD#4, PVD#11 and PIB#1) demonstrate MTFs that are relatively close to the theoretical limit at low spatial frequencies. These results are superior to that obtained from a direct

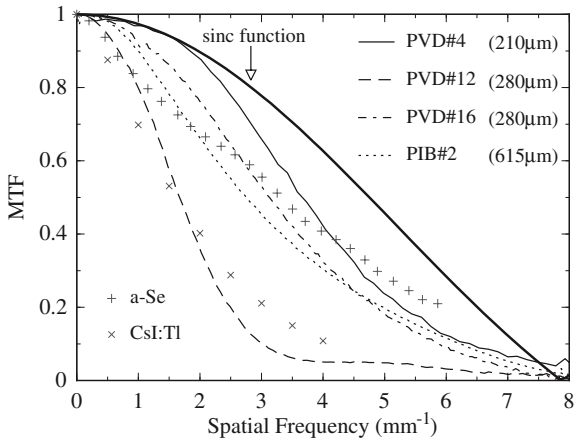

Figure 10. Presampled MTF measured from four prototype arrays, PVD#4 (thin solid line), PVD#12 (dashed line), PVD#16 (dot-dashed line) and PIB#2 (dotted line). The graph also shows the sinc function corresponding to the 127 μm pixel pitch of the arrays (thick solid line). The MTF of a direct detection AMFPI with a 1000 μm thick a-Se detector (plus symbols), along with the MTF for an indirect detection AMFPI with a CsI:Tl detector (cross symbols), are also shown. The a-Se and CsI:Tl results are based on reported MTFs (Hunt *et al* 2004, Granfors *et al* 2003), modified so as to correspond to the results expected for 127 μm pitch arrays with signal collection fill factors of 100% and 80%, respectively.

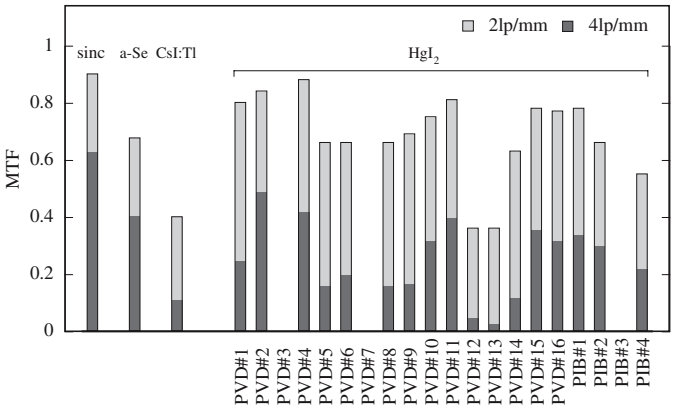

Figure 11. MTF values obtained from those prototype arrays that offered a block of properly functioning pixels sufficiently large for measurement of this quantity. Results are shown in the form of a bar chart. For a given prototype, the MTF at 2 and 4 lp mm^{-1} is indicated by the top of the lighter and darker shaded portions of the bar, respectively. Values are also shown for a sinc function with an aperture of 127 μm, corresponding to the theoretical upper limit of MTF imposed by the design of the array. In addition, MTF values for a 127 μm pitch AMFPI with a-Se and CsI:Tl detectors, derived from published results, and corresponding to the curves shown in figure 10, are included.

detection AMFPI with an a-Se detector having an equivalent x-ray quantum efficiency. Many of the remaining prototypes (including PVD#5 and PIB#4) demonstrate a somewhat lower level of MTF, which is nevertheless substantially higher than for the indirect detection AMFPI with CsI:Tl. Finally, yet other prototypes (including PVD#12, PVD#13 and PVD#14) exhibit

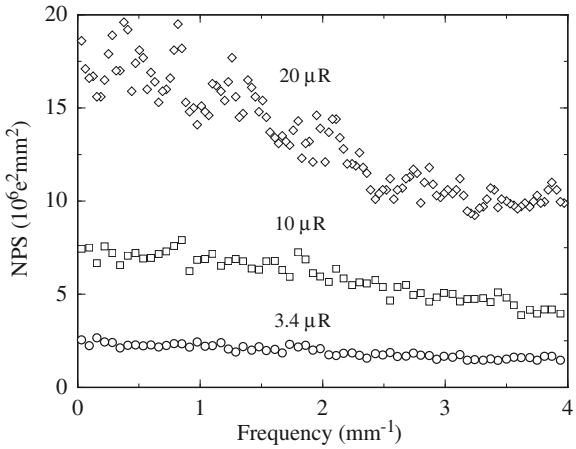

Figure 12. NPS results obtained empirically at several exposures for prototype PVD#4. Note that a gain correction, of the same type used in the non-uniformity studies, has been applied in the data analysis.

relatively poor MTF, only comparable to that of CsI:Tl at some or all spatial frequencies. In the case of PVD#8, PVD#9, PVD#12 and PVD#14, the non-uniformities for these prototypes, after gain correction, were significantly lower than that expected based on x-ray statistics—a seemingly anomalous behavior. Thus, sharing of charge between adjacent pixels, which was suggested in section 3.5 as being responsible for this anomaly, would be expected and, in fact, appears to negatively affect spatial resolution at some or all frequencies. Such charge sharing is very likely due to unintended spread of charges within the photoconductor and/or at the interface between the photoconductor and the pixel electrodes of the array. While the present study was not designed to identify the precise origin of this spreading, some degree of inhibition of charge flow from the photoconductor directly to the underlying pixel collection electrodes at the barrier layer is a possible candidate. Such blocking of charge at the barrier layer of a direct detection AMFPI employing a-Se has been hypothesized as a possible cause of charge sharing and blurring (Zhao *et al* 2003). It is also of interest to note that, even for a prototype with a relatively thick PIB coating, PIB#2, the measured MTF is still significantly higher than that of the CsI:Tl detector. Finally, an x-ray image of a line-pair phantom obtained with PVD#16 (not shown) shows that up to ~3.5 line-pairs mm^{-1} can be resolved, consistent with the pixel pitch of the array, demonstrating the good spatial resolution properties of one of the better-performing prototypes.

3.8. NPS and DQE

Results for NPS and DQE are reported for prototype array PVD#4. Among the prototypes, PVD#4 exhibited the combination of properties most conducive for providing an accurate, and insightful determination of DQE. These properties include: a low level of pixel and line defects; low dark current, dark signal drift and dark (i.e., additive) noise; and high x-ray sensitivity, spatial resolution and linearity of signal response. Figure 12 shows NPS results obtained at x-ray exposures of 3.4, 10 and 20 μR. NPS is observed to increase almost linearly with increasing exposure, indicating that noise is primarily determined by the statistics of the incident x-rays. Furthermore, for a given exposure, NPS exhibits a weak dependence

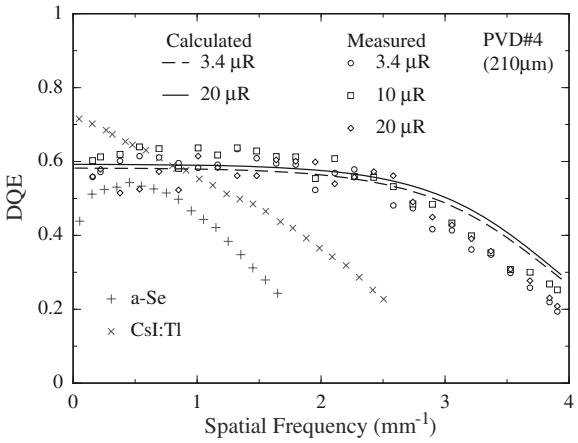

Figure 13. Frequency-dependent DQE results for prototype PVD#4 at 3.4, 10 and 20 μR (circle, square and diamond symbols, respectively). These results correspond to DQE values determined experimentally using the NPS values reported in figure 12. For clarity of presentation, each plotted data point represents an average of the measured DQE over a frequency interval of $\sim$0.16 lp mm^{-1}. The dashed and solid lines correspond to cascaded systems calculations of the DQE at 3.4 and 20 μR, respectively. Finally, the cross and plus symbols correspond to DQE values reported for a 300 and 200 μm pitch direct and indirect detection AMFPIs with a-Se and CsI:Tl detectors, measured with an x-ray spectrum similar to that used in the present study, at 4.4 and 3 μR, respectively (Hunt *et al* 2004, Granfors *et al* 2003).

on spatial frequency, indicating a weak correlation of noise between pixels—a result that is consistent with the good MTF exhibited by PVD#4.

Figure 13 shows results of DQE empirically determined at x-ray exposures of 3.4, 10 and 20 μR. The results overlap, indicating exposure independence under these conditions. This is a clear indication that the prototype is input-quantum-limited for the reported exposures—i.e., the performance is limited only by the x-ray quantum noise and not by other noise factors. Theoretical values of DQE calculated for this prototype at exposures of 3.4 and 20 μR, using a cascaded systems analysis, are also shown in the figure. These calculations were performed using the parameters given in figure 2. The magnitude and spatial frequency dependence of the measured DQE values are in good agreement with the theoretical values, other than for a relatively small discrepancy at high spatial frequencies (i.e. above 2.5 lp mm^{-1}). The observed difference may be the result of an underestimation of the photoconductor MTF, T_3, both in the calculated and in the empirically determined DQE results. Since T_3 was derived from measured system MTF obtained at much higher ($\sim$10 times) pixel signal levels than that used in the NPS measurements, it might not be representative of the resolution at lower signal levels where the MTF may be better. (Accurate determination of MTF at lower signal levels was not experimentally possible.)

Overall, at low spatial frequencies the DQE is dominated by the x-ray quantum efficiency ($\sim$0.64) and the Swank factor ($\sim$0.93) of the photoconductor. For comparison, the DQE performance of direct and indirect detection AMFPIs with a-Se and CsI:Tl detectors, respectively, obtained under similar irradiation conditions, are also plotted in figure 13. These direct and indirect detection AMFPIs were operated at effective pixel pitches of 300 and 200 μm, leading to a factor of $\sim$5.6 and $\sim$2.5 enhancement in x-ray signal, respectively, compared to PVD#4 (127 μm pixel pitch). Despite a smaller pixel pitch, PVD#4 demonstrates a slower fall off in DQE with increasing spatial frequency. This favorable behavior is due to the comparatively larger SNR, as well as higher spatial resolution, provided by the HgI_2

photoconductor. At low spatial frequencies, PVD#4 exhibits higher DQE values compared to the a-Se AMFPI despite similarities in their respective x-ray quantum efficiencies. In comparison with the CsI:Tl AMFPI, PVD#4 exhibits lower DQE values due to the fact that the HgI_2 photoconductor is only $\sim$210 μm for this prototype, leading to a lower x-ray quantum efficiency.

Finally, measurements of DQE beyond 20 μR (not shown in figure 13) were observed to decrease with increasing exposure, an effect arising from increases in NPS that are beyond those accounted for by x-ray quantum noise or additive noise. The underlying reason for this unexpected trend (which was also observed for other, less highly performing prototypes) is not understood, but could possibly be related to unusual behaviors, previously discussed in sections 3.3 and 3.5, observed at higher exposures (i.e., polarization and anomalous temporal variation in x-ray signal response from pixel to pixel, respectively).

4. Summary and discussion

In this paper, we have reported a detailed investigation of the properties and performance of direct detection, active matrix flat-panel arrays coated with two forms of polycrystalline HgI_2 photoconductor. The fundamental motivation for pursuing development of this material is the fact that, for the single-crystal form of the material, the amount of energy required for producing each electron–hole pair, $\sim$4.2 eV, is substantially less than that of the detectors used in conventional AMFPIs. Our research into polycrystalline forms of HgI_2 is driven by the expectation that this form of the material (which lends itself to large area deposition, unlike the single crystal form) will exhibit similar levels of sensitivity, thereby providing $\sim$5 to 10 times as much signal per x-ray than the more commonly used CsI:Tl and a-Se detectors.

In this context, the results obtained from some of the prototype arrays are encouraging. For PVD, low values for W_{EFF} (ranging from $\sim$6.0 to 9.6 eV) were observed for about two-thirds of the prototypes. Moreover, these values were obtained with electric field strengths across the photoconductor below 1 V μm^{-1} —i.e., less than one tenth that used for a-Se. In addition, a few of the PVD prototypes exhibited dark current values that approached, or were below the upper limit of $\sim$1 pA mm^{-2} that is desirable for good AMFPI operation. In addition, the MTF for some of the prototypes was found to approach the limits imposed by x-ray energy deposition and the pitch of the array. It is, however, notable that no one prototype in this study exhibited a combination of very low W_{EFF}, low dark current and high MTF. Nevertheless, it is very positive that DQE performance limited only by the noise associated with x-ray statistics was observed for an exposure down to 3.4 μR, the lowest value that was experimentally accessible in this study and a value that corresponds to an average fluoroscopic exposure.

Conversely, a variety of undesirable behaviors were also observed among the PVD prototypes. Considerable variation in all measured properties was observed from prototype to prototype, despite efforts to converge toward low W_{EFF}, dark current and high MTF. This suggests that the properties of the PVD material may be quite sensitive to even small perturbations in some of the detector fabrication parameters (e.g. barrier conductivity). Furthermore, reductions in charge trapping, lag and the degree of non-uniformity in pixel signal response, from the levels observed in this study, are desirable. Charge trapping in electronic states in the HgI_2 was, in most cases, well beyond 20%, and represents a substantial loss of signal for radiographic mode operation. In addition, a different form of charge trapping, most likely at the interface of the barrier layer and the HgI_2, was observed to result in polarization effects—reducing fluoroscopic sensitivity as well as the range of linear behavior of the x-ray signal response. The rather high level of non-uniformity in the pixel signal response observed

for many prototypes (up to ∼50%) reduces the maximum exposure at which a prototype may be operated in order to avoid saturation of a substantial fraction of the pixels. In addition, although the application of a simple gain correction usually resulted in a substantial reduction of non-uniformity, about one-third of the prototypes exhibited evidence of charge sharing between pixels while another one-third exhibited indications of anomalous temporal variation in the x-ray signal response from pixel to pixel. The presence of charge sharing should reduce spatial resolution, and the MTF results show a degree of consistency with this expectation. Temporal variation in the x-ray signal response would reduce object detectability, since the gain correction would not be as effective in reducing spatial noise created by this variation.

In the case of PIB, W_{EFF} values of ∼22–33 eV were observed—far above that of the PVD prototypes and of results observed from simple, non-pixelated PIB film detectors (Su *et al* 2005). For these detectors, the reported W_{EFF} values measured radiographically were ∼13 eV and were obtained from a pair of detectors having thicknesses of 320 and 458 μm. Although the underlying cause for the higher values of W_{EFF} observed from the PIB prototypes is not well understood, it may be a consequence of less efficient charge transport across the generally thicker photoconductive material in these prototypes. Encouragingly, dark current for all the PIB prototypes was relatively small, and these results included the two lowest values observed in the study. In addition, the MTF of two of the PIB prototypes were relatively high. However, some of the undesirable behaviors noted above for PVD, related to charge trapping and non-uniformity in pixel signal response, were also observed for the PIB prototypes.

Two other behaviors observed during the course of our study are noteworthy. First, while the properties of the evaluated prototypes were generally found to be stable over the one to two months required for measurements following photoconductor deposition, subsequent follow-up measurements performed on some of the PVD prototypes several years later indicated degradation of ∼10%–70% in x-ray sensitivity. (Such loss of sensitivity was not observed for PIB prototypes.) A possible explanation for this change could be insufficient encapsulation of the detector—which could allow oxygen to penetrate into the photoconductor thereby compromising its purity and behavior. Alternatively, it is conceivable that room-temperature annealing of the PVD material over extended periods of time may affect the polycrystalline structure in such a way as to reduce sensitivity.

Second, throughout the study, chemical reactions between the HgI_2 and aluminum in the arrays occurred across the surface of some of the prototypes. While the frequency and extent of these occurrences decreased greatly as the study progressed, they were never completely eliminated. Since the aluminum is deeply embedded in the structure of the arrays, such reactions imply the presence of imperfections in both the barrier layers as well as in the passivation layer on the surface of the uncoated arrays—allowing HgI_2 to penetrate and begin reacting. Since elimination of all aluminum from the arrays is difficult (due to the lack of a viable alternative having the same desirable properties), complete elimination of this problem requires one, or a combination, of (a) improved surface passivation of the arrays—free of the voids and particulate contamination that are likely pathways for HgI_2 to enter the array structure; (b) an alternative to the polymer-based barrier approach that has, even after considerable effort, been unable to completely and reliably contain the HgI_2.

The present study opens up many interesting questions about the physical mechanisms responsible for the observed behaviors. For example, there are interesting questions about the nature of charge trapping in the material (e.g., electron versus hole contributions; trapping occurring at grain boundaries, at barrier interfaces, or from deep traps in the bulk material due to Hg or I vacancies). In addition, there are equally complex and interesting questions concerning the origin of the charge sharing that leads to relatively poor MTF and other effects. Investigations of such questions would benefit from carefully designed, highly focused studies

that would involve examinations of signals from simple, non-pixelated film detectors, as well as from the more complex signal environment of array prototypes. The present study illuminates both the promise and the challenges associated with development of polycrystalline HgI_2 for x-ray imaging applications. The present study also illuminates that the low values for W_{EFF} observed from many of the PVD prototypes clearly favor the use of this form of the material for applications, such as low-exposure-per-frame fluoroscopy, requiring high x-ray sensitivity. On the other hand, while the PIB form of HgI_2 exhibits substantially higher values for W_{EFF} (comparable to that of CsI:Tl), it appears to more consistently achieve low dark current levels—consistent with earlier findings from simple film detectors (Su *et al* 2005). Given that PIB fabrication is simpler and much faster than for PVD (which involves long deposition times and a vacuum reactor), PIB is an attractive candidate for applications requiring thick detectors, but not high x-ray sensitivity. For example, the quantum efficiency and DQE performance of radiotherapy imagers could potentially benefit from high atomic number, relatively high density, thick (in excess of 5 mm) PIB detectors, and is under investigation by our group.

Acknowledgments

The authors wish to thank Mr Douglas Berry and Mr Martin Koniczek for assistance with the study, Dr Haim Gilboa from RTR for helpful discussions on HgI_2 deposition, Dr William Yao and Dr Richard L Weisfield from dpiX for explanations of the structure of the ND10 and MD88 arrays, and Dr Robert Street from Palo Alto Research Center for many insightful conversations. This work was supported by NIH grant R01-EB000558.

References

Alexiev D, Dytlewski N, Reinhard M I and Mo L 2004 Characterisation of single-crystal mercuric iodide *Nucl. Instrum. Methods Phys. Res.* A **517** 226–9

Antonuk L E, Boudry J, Huang W, McShan D L, Morton E J, Yorkston J, Longo M J and Street R A 1992a Demonstration of megavoltage and diagnostic x-ray imaging with hydrogenated amorphous silicon arrays *Med. Phys.* **19** 1455–66

Antonuk L E, Boudry J M, Kim C W, Longo M, Morton E J, Yorkston J and Street R A 1991 Signal, noise, and readout considerations in the development of amorphous silicon photodiode arrays for radiotherapy and diagnostic x-ray imaging *Proc. SPIE* **1443** 108–19

Antonuk L E, El-Mohri Y, Huang W, Jee K W, Siewerdsen J H, Maolinbay M, Scarpine V E, Sandler H and Yorkston J 1998 Initial performance evaluation of an indirect-detection, active matrix flat-panel imager (AMFPI) prototype for megavoltage imaging *Int. J. Radiat. Oncol. Biol. Phys.* **42** 437–54

Antonuk L E, El-Mohri Y, Siewerdsen J H, Yorkston J, Huang W, Scarpine V E and Street R A 1997 Empirical investigation of the signal performance of a high-resolution, indirect detection, active matrix flat-panel imager (AMFPI) for fluoroscopic and radiographic operation *Med. Phys.* **24** 51–70

Antonuk L E *et al* 2005 Investigation of strategies to achieve optimal DQE performance from indirect-detection active-matrix flat-panel imagers (AMFPIs) through novel pixel amplification architectures *Proc. SPIE* **5745** 18–31

Antonuk L E, Jee K W, El-Mohri Y, Maolinbay M, Nassif S, Rong X, Zhao Q, Siewerdsen J H, Street R A and Shah K S 2000 Strategies to improve the signal and noise performance of active matrix, flat-panel imagers for diagnostic x-ray applications *Med. Phys.* **27** 289–306

Antonuk L E, Yorkston J, Huang W, Boudry J, Morton E J, Longo M J and Street R A 1992b Factors affecting image quality for megavoltage and diagnostic x-ray a-Si:H imaging arrays *Mater. Res. Soc. Symp. Proc.* **258** 1069–74

Antonuk L E, Zhao Q, Su Z, Yamamoto J, El-Mohri Y, Li Y, Wang Y and Sawant A R 2004 Systematic development of input-quantum-limited fluoroscopic imagers based on active matrix, flat-panel technology *Proc. SPIE* **5368** 127–38

Boone J M and Seibert J A 1997 An accurate method for computer-generating tungsten anode x-ray spectra from 30 to 140 kV *Med. Phys.* **24** 1661–70

Cunningham I A and Shaw R 1999 Signal-to-noise optimization of medical imaging systems *J. Opt. Soc. Am.* A **16** 621–32

Cunningham I A, Westmore M S and Fenster A 1994 A spatial-frequency dependent quantum accounting diagram and detective quantum efficiency model of signal and noise propagation in cascaded imaging systems *Med. Phys.* **21** 417–27

El-Mohri Y, Antonuk L E, Zhao Q, Wang Y, Li Y, Du H and Sawant A 2007 Performance of a high fill factor, indirect detection prototype flat-panel imager for mammography *Med. Phys.* **34** 315–27

El-Mohri Y, Jee K W, Antonuk L E, Maolinbay M and Zhao Q 2001 Determination of the detective quantum efficiency of a prototype, megavoltage indirect detection, active matrix flat-panel imager *Med. Phys.* **28** 2538–50

Fujita H, Tsai D Y, Itoh T, Doi K, Morishita J, Ueda K and Ohtsuka A 1992 A simple method for determining the modulation transfer-function in digital radiography *IEEE Trans. Med. Imaging* **11** 34–9

Granfors P R and Aufrichtig R 2000 DQE(f) of an amorphous silicon flat panel x-ray detector: detector parameter influences and measurement methodology *Proc. SPIE* **3977** 2–13

Granfors P R, Aufrichtig R, Possin G E, Giambattista B W, Huang Z S, Liu J and Ma B 2003 Performance of a 41×41 cm^2 amorphous silicon flat panel x-ray detector designed for angiographic and R&F imaging applications *Med. Phys.* **30** 2715–26

Hartsough N E, Iwanczyk J S, Patt B E and Skinner N L 2004 Imaging performance of mercuric iodide polycrystalline films *IEEE Nucl. Sci.* **51** 1812–6

Huang W, Antonuk L E, Berry J, Maolinbay M, Martelli C, Mody P, Nassif S and Yeakey M 1999 An asynchronous, pipelined, electronic acquisition system for active matrix flat-panel imagers (AMFPIs) *Nucl. Instrum. Methods Phys. Res.* A **431** 273–84

Hunt D C, Tanioka K and Rowlands J A 2007 X-ray imaging using avalanche multiplication in amorphous selenium: Investigation of depth dependent avalanche noise *Med. Phys.* **34** 976–86

Hunt D C, Tousignant O and Rowlands J A 2004 Evaluation of the imaging properties of an amorphous selenium-based flat panel detector for digital fluoroscopy *Med. Phys.* **31** 1166–75

Jaffray D A, Battista J J, Fenster A and Munro P 1995 Monte-Carlo studies of x-ray-energy absorption and quantum-noise in megavoltage transmission radiography *Med. Phys.* **22** 1077–88

Jee K W, Antonuk L E, El-Mohri Y and Zhao Q 2003 System performance of a prototype flat-panel imager operated under mammographic conditions *Med. Phys.* **30** 1874–90

Karim K S, Nathan A and Rowlands J A 2003 Amorphous silicon active pixel sensor readout circuit for digital imaging *IEEE Trans. Electron. Devices* **50** 200–8

Maolinbay M, El-Mohri Y, Antonuk L E, Jee K W, Nassif S, Rong X and Zhao Q 2000 Additive noise properties of active matrix flat-panel imagers *Med. Phys.* **27** 1841–54

Matsuura N, Zhao W, Huang Z and Rowlands J A 1999 Digital radiology using active matrix readout: amplified pixel detector array for fluoroscopy *Med. Phys.* **26** 672–81

Nelson W R and Rogers D W O 1989 *Monte Carlo Transport of Electrons and Photons Below 50 MeV* ed Jenkins T M *et al* (New York: Plenum) pp 287–306

Rieppo P K and Rowlands J A 1997 X-ray imaging with amorphous selenium: theoretical feasibility of the liquid crystal light valve for radiography *Med. Phys.* **24** 1279–91

Samei E and Flynn M J 2003 An experimental comparison of detector performance for direct and indirect digital radiography systems *Med. Phys.* **30** 608–22

Schieber M *et al* 2000 Mercuric iodide thick films for radiological x-ray detectors *Proc. SPIE* **4142** 197–204

Schieber M *et al* 2001 Thick films of X-ray polycrystalline mercuric iodide detectors *J. Cryst. Growth* **225** 118–23

Schieber M, Hermon H, Zuck A, Vilensky A, Melekhov L, Shatunovsky R, Meerson E and Saado Y 1999 Polycrystalline mercuric iodide detectors *Proc. SPIE* **3770** 146–55

Schieber M, Zuck A, Braiman M, Nissenbaum J, Turchetta R, Dulinski W, Husson D and Riester J L 1997 Novel mercuric iodide polycrystalline nuclear particle counters *IEEE Trans. Nucl. Sci.* **44** 2571–5

Shaw R 1963 The equivalent quantum efficiency of the photographic process *J. Photogr. Sci.* **11** 199–204

Simon M, Ford R A, Franklin A R, Grabowski S P, Menser B, Much G, Nascetti A, Overdick M, Powell M J and Wiechert D U 2005 Analysis of lead oxide (PbO) layers for direct conversion x-ray detection *IEEE Trans. Nucl. Sci.* **52** 2035–40

Street R A, Nelson S, Antonuk L E and Perez-Mendez V 1990 Amorphous silicon sensor arrays for radiation imaging *Mater. Res. Soc. Symp. Proc.* **192** 441–52

Street R A, Ready S E, van Schuylenbergh K, Ho J, Boyce J B, Nylen P, Shah K, Melekhov L and Hermon H 2002 Comparison of PbI2 and HgI2 for direct detection active matrix x-ray image sensors *J. Appl. Phys.* **91** 3345–55

Su Z, Antonuk L E, El-Mohri Y, Hu L, Du H, Sawant A, Li Y, Wang Y, Yamamoto J and Zhao Q 2005 Systematic investigation of the signal properties of polycrystalline HgI2 detectors under mammographic, radiographic, fluoroscopic and radiotherapy irradiation conditions *Phys. Med. Biol.* **50** 2907–28

Vedantham S *et al* 2000 Full breast digital mammography with an amorphous silicon-based flat panel detector: physical characteristics of a clinical prototype *Med. Phys.* **27** 558–67

Yarema R J, Zimmerman T, Srage J, Antonuk L E, Berry J, Huang W and Maolinbay M 2000 A programmable, low noise, multichannel ASIC for readout of pixelated amorphous silicon arrays *Nucl. Instrum. Methods Phys. Res.* A **439** 413–7

Zentai G, Partain L and Pavlyuchkova R 2007 Dark current and DQE improvements of mercuric iodide medical imagers *Proc. SPIE* **6510** 65100Q-1–6

Zentai G, Partain L, Pavlyuchkova R, Virshup G F, Zuck A, Melekhov L, Dagan O, Vilensky A and Gilboa H 2002 Large-area mercuric iodide x-ray imager *Proc. SPIE* **4682** 592–600

Zhao B and Zhao W 2003 Characterization of a direct, full-field flat-panel digital mammography detector *Proc. SPIE* **5030** 157–67

Zhao W, Ji W G, Debrie A and Rowlands J A 2003 Imaging performance of amorphous selenium based flat-panel detectors for digital mammography: characterization of a small area prototype detector *Med. Phys.* **30** 254–63

Zhao W, Li D, Reznik A, Lui B J M, Hunt D C, Rowlands J A, Ohkawa Y and Tanioka K 2005 Indirect flat-panel detector with avalanche gain: fundamental feasibility investigation for SHARP-AMFPI (scintillator HARP active matrix flat panel imager) *Med. Phys.* **32** 2954–66

Zhao W and Rowlands J A 1995 X-ray imaging using amorphous selenium: feasibility of a flat panel self-scanned detector for digital radiology *Med. Phys.* **22** 1595–604

Zuck A, Schieber M, Khakhan O and Burshtein Z 2003 Near single-crystal electrical properties of polycrystalline HgI2 produced by physical vapor deposition *IEEE Trans. Nucl. Sci.* **50** 991–7